

VISCOUS SHOCK-LAYER PREDICTIONS OF THREE-DIMENSIONAL NONEQUILIBRIUM
FLOWS PAST THE SPACE SHUTTLE AT HIGH ANGLE OF ATTACK

M. D. Kim, S. Swaminathan, and Clark H. Lewis
Aerospace and Ocean Engineering Department
Virginia Polytechnic Institute and State University
Blacksburg, Virginia

SUMMARY

Computational solutions have been obtained for chemically reacting flowfields over the entire windward surface of the Space Shuttle at high angle-of-attack. The recently developed computational method for the Space Shuttle is capable of treating three-dimensional viscous nonequilibrium air flow as well as equilibrium air and perfect gas flows. A general nonorthogonal computational grid system is used to treat the nonaxisymmetric geometry. Boundary conditions take into account noncatalytic wall, equilibrium catalytic wall, and shock and wall slip conditions. The nonequilibrium solutions with noncatalytic wall condition are compared to the fully catalytic wall solutions, the equilibrium air solutions, the perfect gas solutions, and also the Shuttle flight heating and pressure data. The comparisons show good agreements and correlations in most cases.

INTRODUCTION

Recently the nonequilibrium effect on the Shuttle reentry flowfield has been widely investigated to reduce the surface heating by employing a proper surface material. The purpose of the present paper is to accurately predict the three-dimensional nonequilibrium flowfield over the entire Shuttle windward surface and compare the result with the flight data of heating rate and pressure. For a few typical reentry flight conditions, the nonequilibrium solutions were obtained for both noncatalytic and fully catalytic wall conditions, and compared with the corresponding equilibrium and perfect gas solutions. The present numerical scheme was also extended to include the capability to treat the nonequilibrium wall and shock slip conditions.

The present numerical method (SHTNEQ) has been developed based on the two-dimensional nonequilibrium flowfield code by Miner and Lewis (ref. 1) and the three-dimensional perfect gas code by Szema and Lewis (ref. 2). The complete governing equations and the description of the present method are given by Kim, Swaminathan and Lewis (ref. 3). The SHTNEQ method uses a general nonorthogonal computational grid system to treat the nonaxisymmetric Shuttle geometry. Since the three-dimensional viscous shock-layer equations are parabolic in both the streamwise and crossflow directions, the equations are solved by a highly efficient finite-difference scheme developed by Murray and Lewis (ref. 4), which requires much less computing time than PNS or time-dependent methods. The present method can solve both subsonic and super-

sonic flows and requires the shock shape as initial input data. The shock shapes for the present Shuttle calculations were provided by the inviscid HALIS method of Weilmuenster and Hamilton (ref. 5).

In the later sections, a description of the governing equations and boundary conditions is given, and the thermodynamic properties and chemical reaction model used in the present calculations are also described. It is known that the nonequilibrium real gas effects persist through a wide range of the Shuttle reentry trajectory (altitudes of 122 to 50 km). In the present work, three points along the trajectory of the second Space Shuttle flight (STS-2) are chosen, and the numerical solutions are obtained over the entire windward surface of the body. These freestream conditions are the same as used in ref. 3, and the present paper is an extension of the previous paper by including more calculations with comparisons to additional flight data and also the wall and shock slip effects. The computational results of the surface heating rate and pressure predictions are compared with the STS-2 flight data. The variations of some shock-layer profiles along the body are also presented.

SYMBOLS

C_p	specific heat at constant pressure
FULCAT	nonequilibrium solution with fully catalytic wall
ξ_1	vector in streamwise (ξ_1) direction
ξ_2	vector in normal (ξ_2) direction
ξ_3	vector in circumferential (ξ_3) direction
L	Shuttle body total length, 32.84 m
M_∞	freestream Mach number
NONCAT	nonequilibrium solution with noncatalytic wall
NONEQL	nonequilibrium flow calculation
NSH	shock-layer thickness nondimensionalized by R_n
p	pressure, $p^*/(\rho_\infty U_\infty^2)$
PG	perfect gas solution
PHI	same as ϕ in cylindrical coordinates
PW/PINF	same as p_w/p_∞
QW	surface heating rate due to conduction and diffusion (MW/m^2)
Re_x	freestream unit Reynolds number, m^{-1}
R_n	dimensional Shuttle nose radius, 62.23 cm (24.5 inches)

SHTNEQ Shuttle nonequilibrium, the present numerical method
 STS space transportation system
 S/RN surface distance along body nondimensionalized by R_n
 T temperature, T^*/T_{ref}
 T_{ref} dimensional reference temperature, $U_\infty^2/C_{p\infty}$
 t Shuttle entry time from 122 km altitude
 U_∞ dimensional freestream velocity
 u,v,w streamwise, normal and circumferential velocity tensor components
 nondimensionalized by U_∞
 U/UINF streamwise velocity, u^*/U_∞
 \dot{w}_i species production term
 Y/RN body-normal distance nondimensionalized by R_n
 z,r, ϕ reference cylindrical coordinates
 Z/L axial distance along body, same as z/L
 α angle of attack, degree
 ϵ Reynolds number parameter, $[\mu_{ref}/(c_\infty U_\infty R_n)]^{1/2}$
 μ viscosity, μ^*/μ_{ref}
 μ_{ref} reference viscosity evaluated at T_{ref}
 ξ_1, ξ_2, ξ_3 computational coordinates
 ρ density, ρ^*/ρ_∞

Superscript

* dimensional quantity

Subscript

i species i
 w wall value
 ∞ dimensional freestream value

ANALYSIS

Governing Equations

The governing equations are derived from the steady Navier-Stokes equations for a reacting gas mixture as given by Bird et al. (ref. 6), and they are written in a surface-oriented general nonorthogonal coordinate system (see fig. 1). The ξ_1 coordinate consists of straight lines in the surface-normal direction. At the body surface, the ξ_3 coordinate is chosen to coincide with the ϕ coordinate of the reference cylindrical coordinate system. The coordinate system requires orthogonality only at the body surface. The normal velocity v and normal coordinate ξ_2 are assumed to be the order of ϵ , and all terms which are of higher order than ϵ are neglected in the governing equations. The local physical velocity vector is defined as

$$\underline{V} = u\underline{g}_1 + v\underline{g}_2 + w\underline{g}_3$$

where the u , v and w are tensor velocity components in the computational coordinate system. Only laminar flow is considered in the present analysis. The derived nondimensional form of the three-dimensional viscous shock-layer equations for a reacting gas mixture is given in ref. 3.

Boundary Conditions

At the body surface, the slip and temperature-jump boundary condition can be used if necessary. The nonequilibrium wall slip equations given by Hendricks (ref. 7) have been rewritten for the present coordinate system and chemical model. The calculated Reynolds number parameter ϵ was less than 0.108 for the present test cases which indicates that the slip effects on the heating rate and surface pressure will be small (see e.g. ref 8), but the slip effects on some shock-layer profiles over the nose region are calculated and presented. The wall temperature is specified by the STS-2 flight thermocouple data. In the present calculations, the wall species concentration is dictated by the noncatalytic or fully catalytic condition, but the boundary condition can easily be extended to include the effects of finite wall catalytic on the recombination of dissociated air. At the low surface temperature of Shuttle, the equilibrium catalytic wall condition can be replaced by the fully catalytic wall condition.

In the present method, shock shape information is necessary as an input which is used for the calculation of the shock-boundary condition. The three-dimensional shock-boundary conditions with slip effects (modified Rankine-Hugoniot jump relations) given by Murray and Lewis (ref. 4) have been extended to include finite-rate chemistry and the nonorthogonal coordinate system. Two-dimensional shock-normal coordinates are defined in the plane which contains both the freestream velocity vector and the vector which is normal to the local shock surface. Then, the freestream velocity vector is written in the shock-normal coordinates, and two-dimensional shock-crossing conditions are calculated in the shock-normal coordinates. The known after-shock quantities are rotated into the three-dimensional computational coordinates.

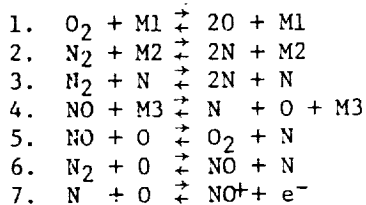
Thermodynamic and Transport Properties

Multi-component ionizing air is considered to be a mixture of thermally perfect gases, and the thermodynamic and transport properties for each species are calculated

using the local temperature. The properties for the gas mixture are then determined in terms of the individual species properties. The enthalpy and specific heat of each species are obtained from the thermodynamic data tabulated by Browne (refs. 9-11). A second-order Lagrangian method is used to interpolate the values at a given temperature. The viscosity of the individual species is calculated from the curve fit relation given by Blottner (ref. 12), and the thermal conductivity of each species is calculated from the Eucken semi-empirical formula using the species viscosity and specific heat. After the viscosity and thermal conductivity of the individual species are calculated, the viscosity and thermal conductivity of the gas mixture are calculated by the method suggested by Armaly and Sutton (refs. 13, 14). In the present work, the diffusion model is limited to binary diffusion with the binary diffusion coefficient specified by the Lewis number of 1.4.

Chemical Reaction Model

It is assumed that the chemical reactions proceed at a finite rate, and the rate of production terms w_i of the individual species are included in the energy equation and the species continuity equations. The w_i terms are functions of both the temperature and the species concentrations, and they must be rewritten so that the temperature or the species concentrations appear as one of the unknowns as given in ref. 1. In the present calculations, the chemical reaction model and the reaction-rate constants are taken from Blottner (ref. 15). Seven (7) chemical species are considered in the reactions; viz., O, O₂, NO, N, NO⁺, N₂, and e⁻. The following pure air chemical reactions are used for the present study:



where M1, M2 and M3 are the catalytic third bodies (M). Since the rate of production terms are for nonequilibrium flows, the present model encounters difficulty in obtaining a converged solution whenever the flow conditions approach equilibrium. The difficulty is severe, particularly at the stagnation point.

Numerical Solution

Davis (ref. 8) presented an implicit finite-difference method to solve the viscous shock-layer equations for axially symmetric flows, and Murray and Lewis (ref. 4) further developed the scheme for three-dimensional flows. In the present work, the method is extended to the chemically reacting three-dimensional flowfield solution in a surface-oriented nonorthogonal coordinate system. Since the viscous shock-layer equations are parabolic in both the streamwise and crossflow directions, the equations are solved by a highly efficient finite-difference scheme. The continuity and normal momentum equations are solved in a coupled form to promote convergence. The shock stand-off distance is evaluated by integrating the continuity equation.

The solution begins on the spherically blunted nose by obtaining an axisymmetric solution in the wind-fixed coordinate system. The axisymmetric solution is rotated into the body-fixed coordinates and is used as the initial profile for the three-

dimensional solution. The three-dimensional solution begins in the windward plane and marches around the body obtaining a converged solution at each ξ_3 -step. After completing a sweep at a ξ_1 -marching station, the procedure then steps downstream in ξ_1 and begins the next ξ_3 -sweep. At each point the equations are solved in the following order: (i) species continuity, (ii) ξ_3 -momentum, (iii) energy, (iv) ξ_1 -momentum, (v) integration of continuity for shock-layer thickness, and (vi) coupled continuity and normal momentum equations.

RESULTS AND DISCUSSION

In order to predict the Shuttle reentry flowfield, three test cases were chosen and the viscous windward flowfield solutions were obtained using various chemical models. For the wide range of the Shuttle reentry conditions (above 50 km altitude, the nonequilibrium effects can occur, and the nonequilibrium effects are largest near the nose of the body and around $t = 450$ sec on the trajectory (ref. 16). The altitudes selected for the present calculations are 81, 70 and 60 km ($t = 250, 460, 630$ sec, respectively). Detailed freestream conditions for the three test cases are given in table I. The inviscid input shock shapes for the present calculations have been provided by the HALIS method for an angle-of-attack of 40 deg for both perfect gas and equilibrium air. The inviscid HALIS shock was available only up to $z/L = 0.5$ or less. The viscous flowfield solutions for perfect gas and equilibrium air have been obtained up to $z/L = 0.5$ in order to compare with the nonequilibrium solutions. The nonequilibrium solutions, however, were obtained for the entire windward surface up to the body end using an extended shock. The shock extension was done using the STEIN (ref. 17) solution of the shock shape for an angle-of-attack of 25 deg. The extended shock was scaled and smoothed before being used as input data. In order to enhance the accuracy of the nonequilibrium viscous solution, a global iteration has been performed using the viscous output shock as an input.

The nonequilibrium solutions have been obtained for both noncatalytic and fully catalytic wall conditions for the purpose of comparison. The cross-sections of the modified Shuttle orbiter which have been used for the inviscid and viscous solutions are depicted in fig. 2. Presented results include the surface heating rate, surface pressure, shock shapes, a few shock-layer profiles, and finally slip effects over the nose region. The flight heating-rate data obtained from the method by Throckmorton (ref. 18) are used for comparison with the computational results. The flight measurement data of pressure are used for comparison with the present surface-pressure predictions.

Surface Heating Rate

The heating-rate predictions along the windward centerline are compared with each other in fig. 3 for Case 1. The nonequilibrium solution with noncatalytic wall condition agrees well with the flight data for most of the region. The nonequilibrium solution with fully catalytic wall condition shows quite close agreement with the equilibrium air solution. The heating-rate prediction from the perfect gas model is below the equilibrium air solution but well above the noncatalytic wall solution for the entire body. The reason for the local mismatch around $z/L = 0.2$ is not currently known. At $z/L = 0.4$, the perfect gas solution is 20% lower than the equilibrium solution and 50% higher than the noncatalytic wall solution. In fact, the surface finite catalytic effect for Case 1 is negligible compared to that for Cases 2 and 3, due to the altitude dependence of the surface catalytic activity (ref. 19). The decrease of the heating after $z/L = 0.8$ is due to the slope change of the body surface.

For Cases 2 and 3, the general trends of the computed heating rates are similar to the result of Case 1, but the noncatalytic wall solution underpredicts compared to the flight data especially on the nose region and the body-end region as shown in figs. 4 and 5. The discrepancy over those regions may be due to the surface catalytic effect as recently discussed by other investigators (refs. 16, 19 and 20). In fig. 6, the nonequilibrium solution with noncatalytic wall condition along the body is shown for various ϕ -planes, together with the corresponding equilibrium air solution for Case 2. The equilibrium air solution is much higher than the noncatalytic wall solution for all the ϕ -planes. In fig. 6, the surface heating distributions along the body for all the ϕ -planes are shown. The sudden increase of the heating rate at $\phi = 80$ deg and $z/L = 0.5$ is due to the spanwise slope change of the body surface along the body (see fig. 2). At $z/L = 0.6$ and $\phi = 90$ deg, the solution did not converge, due to the severe surface slope change of the wing tip section. The calculated windward spanwise heating rates at two axial stations ($z/L = 0.2$ and $z/L = 0.44$) for Case 2 are shown in fig. 7. The comparisons among the various chemical models show similar trends and correlations for the spanwise heating rate distributions due to the flow expansion around the body. The flight data were available only at the windward centerline ($\phi = 0$ deg), and the data agree well with the noncatalytic wall solution.

Surface Pressure Comparison

In fig. 8 the surface-pressure distribution over the entire Shuttle windward surface is presented together with the available flight data for comparison. The ϕ -planes from 10 deg to 40 deg were omitted on the plot because the results for those planes were almost identical with the result for the windward centerline. The agreement with flight data is good especially on the windward centerline for Cases 2 and 3. In fig. 9 the spanwise surface pressure distributions are shown at two axial stations ($z/L = 0.1$ and $z/L = 0.2$). The present calculation tends to underpredict over the flow expansion region (off the centerline) compared to the flight data (e.g. about 20% underprediction at $\phi = 67$ deg, $z/L = 0.1$). This disagreement may be due to the uncertainty of the flight data. A computation using a smaller ϕ -stepsize may also reduce the discrepancy. The present solution by the SHINEQ method used ϕ -stepsize of 10 deg around the body, and this stepsize may not be small enough for the noncircular cross section of the Shuttle geometry (see fig. 2). If more ϕ -planes than the present 10 planes were included in the computation, the current relatively large storage requirement and computing time would increase accordingly.

Shock-Layer Thickness

A comparison of the shock-layer thickness distributions along the body at the $\phi = 0$ plane which has been obtained from various chemical models is shown in fig. 10. All the viscous shock shape results except the inviscid shock are from the once globally iterated results. When an inviscid input shock is not very accurate, the output shock shape is, in general, different from the input shock. In such a case, a global iteration is necessary in order to refine the entire flowfield solution. Thus, for the present three test cases, all the presented viscous flowfield solutions are from the first global iteration. The inviscid shock is from the HALIS code and was available only up to $z/L = 0.5$ as mentioned earlier. The inviscid HALIS shock for $\alpha = 40$ deg has been extended by the inviscid shock of $\alpha = 25$ deg from the STEIN method. The extended shock was scaled and smoothed, and then used as the input shock data for the initial calculation (zeroth iteration). When the various viscous shock-layer thicknesses are compared to the inviscid perfect gas shock at $z/L = 0.4$, the

viscous perfect gas shock is 86.7%, the nonequilibrium shock is 52.8% and the equilibrium shock is 36.1%. The shock from the fully catalytic wall condition is almost identical to the noncatalytic wall solution.

Comparison of Shock-Layer Profiles

The nonequilibrium flowfield structure of the viscous shock-layer at a few selected axial stations on the windward centerline is depicted for both the noncatalytic and fully catalytic wall conditions in figs. 11-14. The profiles include temperature, tangential velocity and mass fractions of oxygen and nitrogen atoms for Case 2 ($t = 460$ sec). The temperature and velocity profiles in figs. 11 and 12 show that the viscous effects are dominant across the entire shock-layer, especially on the forward part of the body. At the axial station of $z/L = 0.046$ in the plot of temperature profile, the wall temperature gradient of the fully catalytic wall solution is larger than that of the noncatalytic wall solution, which produced a 34% larger conduction heating rate. At the same station the heating rate due to the mass diffusion was 93% of the conduction heating rate in the fully catalytic wall solution. The diffusive heating in the noncatalytic wall case was, of course, negligible. The surface chemical catalyticity has negligible effect on the velocity profile as shown in fig. 12. The mass-fraction profiles of oxygen and nitrogen clearly show the effects of the noncatalytic and fully catalytic wall conditions. In the noncatalytic wall case, the oxygen atom concentration at the wall remains almost constant along the body, while the nitrogen atom concentration is reduced downstream due to more rapid recombination.

Slip Effects

The SHTNEQ method has been further extended to include the shock slip and the wall slip conditions. In high altitude freestream conditions, the conventional frozen shock crossing of Rankine-Hugoniot relations for nonequilibrium flows gives poor prediction of the after-shock quantities. It is known that the slip effects on surface-measurable quantities like heating rate and pressure are significant, especially for reentry bodies with a small nose radius at very high altitude. For the Space Shuttle geometry at the test case freestream conditions, however, the calculated Reynolds number parameter ϵ was less than 0.108 which indicates that the slip effects on the surface-measurable quantities will not be significant (ref. 8). In fig. 15, the shock-slip effects on the temperature profile and mass fraction of oxygen and nitrogen atoms are shown at the stagnation point. The slip temperature at the shock is less than the no-slip temperature by 1500 K. The shock-slip effect on the oxygen mass-fraction distribution across the shock-layer is limited to the region near the bow shock, but for nitrogen the shock-slip effect is propagated all through the shock-layer. Figure 16 shows the wall-slip effects on the surface temperature and axial flow velocity jumps over the nose region for Case 2. The amount of the temperature jump is about 200 K at the stagnation point, and the slip velocity is 0.0056 times the freestream velocity at $S/RN = 0.8$.

Computing Times

The computing times required for the flowfield computations of all the test cases are listed in table II. The computing times are based on an IBM 370/3081 general purpose computer. The nonequilibrium computations took about one and a half hours CPU time for solving the entire Shuttle windward surface. When an input shock

data is not accurate, generally a global iteration is required, thus consuming more computing time than the tabulated one. The computing times for the perfect gas and equilibrium air are for the solution of the first half of the body (up to $z/L = 0.5$). The solution of the perfect gas or equilibrium air flows took relatively small computing times (less than 20% of nonequilibrium case). The axial marching step-sizes are controlled internally in the code considering the number of local iterations taken. A fixed input of 51 or 101 grid points was used in the surface-normal direction and 10 planes were used around the body for the windward surface (10 deg step-size). The leeward surface of the Space Shuttle was not considered, because a solution cannot be obtained by the present method due to strong flow separation. The storage requirement of the present SHTNEQ code is 552 kilo-bites in the IBM 370/3081 computer.

CONCLUSIONS

In general, the computational results of surface heating rate for the three-dimensional nonequilibrium flowfield over the Space Shuttle compare well with the available flight data. The flight heating rate data are higher than the noncatalytic wall solution especially on the nose region and the body end due to the surface finite catalytic effect. The nonequilibrium solution with fully catalytic wall gives quite close agreement with the equilibrium heating rate prediction. The perfect gas solution of surface heating rate is less than the equilibrium solution but higher than the flight data for the entire region. The calculated pressure distribution also shows good agreement with the flight data. The calculated nonequilibrium shock- and wall-slip effects on the heating rate were negligible for the present test cases. The computing times taken for the nonequilibrium calculation are reasonable considering the large size of the computational grid due to the complex Shuttle geometry and the chemical reactions of seven species. Further work is planned to calculate the effects of finite catalytic wall conditions on the three-dimensional nonequilibrium flowfield.

REFERENCES

1. Miner, E. W. and Lewis, C. H.: "Hypersonic Ionizing Air Viscous Shock-Layer Flows over Nonanalytic Blunt Bodies," NASA CR-2550, May 1975.
2. Szema, K. Y. and Lewis, C. H.: "Three-Dimensional Viscous Shock-Layer Flows over Lifting Bodies at High Angles of Attack," AIAA Paper No. 81-1146, June 1981.
3. Kim, M. D., Swaminathan, S., and Lewis, C. H.: "Three-Dimensional Nonequilibrium Viscous Shock-Layer Flow over the Space Shuttle Orbiter," AIAA Paper No. 83-0487, Jan. 1983.
4. Murray, A. L. and Lewis, C. H.: "Hypersonic Three-Dimensional Viscous Shock-Layer Flow over Blunt Bodies," AIAA Journal, Vol. 16, No. 12, pp. 1279-1286, Dec. 1978.
5. Weilmuenster, K. James and Hamilton, H. Harris, II: "A Method for Computation of Inviscid Three-Dimensional Flow over Blunt Bodies Having Large Embedded Subsonic Regions," AIAA Paper No. 81-1203, June 1981.
6. Bird, R. B., Stewart, W. E. and Lightfoot, E. N.: Transport Phenomena, John Wiley and Sons, Inc., 1960.

7. Hendricks, W. L.: "Slip Conditions with Wall Catalysis and Radiation for Multicomponent Nonequilibrium Gas Flow," NASA TM X-64942, June 1974.
8. Davis, R. T.: "Numerical Solution of the Hypersonic Viscous Shock-Layer Equations," AIAA Journal, May 1970, pp. 843-851.
9. Browne, W. G., "Thermodynamic Properties of Some Atoms and Atomic Ions," MSD Engineering Physics TM2, General Electric Co., Philadelphia, PA, 1962.
10. Browne, W. G.: "Thermodynamic Properties of Some Diatomic and Linear Polyatomic Molecules," MSD Engineering Physics TM3, General Electric Co., Philadelphia, PA, 1962.
11. Browne, W. G.: "Thermodynamic Properties of Some Diatoms and Diatomic Ions at High Temperature," MSD Advanced Aerospace Physics TM8, General Electric Co., Philadelphia, PA, May 1962. . . .
12. Blottner, F. G.: "Non-equilibrium Laminar Boundary-Layer Flow of Ionized Air," General Electric Report R64SD56, November 1964.
13. Armaly, B. F. and Sutton, K.: "Viscosity of Multicomponent Partially Ionized Gas Mixtures Associated with Jovian Entry," Aerothermodynamics and Planetary Entry, Progress in Astronautics and Aeronautics, Vol. 77, edited by A. L. Crosbie, AIAA, New York, 1981, pp. 335-350.
14. Armaly, B. F. and Sutton, K.: "Thermal Conductivity of Partially Ionized Gas Mixtures," Thermophysics of Atmospheric Entry, Progress in Astronautics and Aeronautics, Vol. 82, edited by Thomas E. Horton, AIAA, New York, 1982, pp. 53-67.
15. Blottner, F. G., Johnson, M., and Ellis, M.: "Chemically Reacting Viscous Flow Program for Multi-Component Gas Mixtures," Sandia Laboratories Report SC-RR-70-754, Dec. 1971.
16. Rakich, J. V., Steward, D. A., and Lanfranco, M. J.: "Results of a Flight Experiment on the Catalytic Efficiency of the Space Shuttle Heat Shield," AIAA Paper No. 82-0944, June 1982.
17. Marconi, F. and Yaeger, L.: "Development of a Computer Code for Calculating the Steady Super/Hypersonic Inviscid Flow Around Real Configurations." NASA CR-2675, April 1976.
18. Throckmorton, D. A.: "Benchmark Aerodynamic Heat Transfer Data from the First Flight of the Space Shuttle Orbiter," AIAA Paper No. 82-0003, Jan. 1982.
19. Shinn, J. L., Moss, J. N. and Simmonds, A. L.: "Viscous Shock-Layer Heating Analysis for the Shuttle Windward Plane with Surface Finite Catalytic Recombination Rates," AIAA Paper No. 82-0842, June 1982.
20. Scott, C. D. and Derry, S. M.: "Catalytic Recombination and the Space Shuttle Heating," AIAA Paper No. 82-0841, June 1982.

TABLE I. TEST CASE FREESTREAM CONDITIONS

Case No.	t (sec)	Altitude (km)	α (deg)	M_∞	Re_∞ (m^{-1})	U_∞ (km/s)	T_∞ (K)	p_∞ (atm)
1	250	85.74	41.0	26.6	2726.	7.53	199.	3.587E-06
2	460	74.98	40.0	25.5	15686.	7.20	198.	2.142E-05
3	650	71.29	39.4	23.4	25756.	6.73	205.	3.965E-05

TABLE II. COMPUTING TIMES^a FOR TEST CASES

Flow Model	Case No.	z/L from - to	Grid Size of			CPU Time (H:M:S)
			ξ_1 -steps	ξ_2 -pts	ξ_3 -planes	
Nonequilibrium Noncatalytic	1	0. - 0.93	127	51	10	1:20:34
	2	0. - 0.93	129	51	10	1:50:28
	3	0. - 0.93	142	51	10	1:51:40
Nonequilibrium Fully Catalytic	1	0. - 0.93	123	51	10	1:23:02
	2	0. - 0.93	124	51	10	1:26:53
	3	0. - 0.93	124	51	10	1:27:22
Perfect Gas	1	0. - 0.50	78	101	10	0:07:07
	2	0. - 0.50	78	101	10	0:07:06
	3	0. - 0.50	78	101	10	0:07:05
Equilibrium	1	0. - 0.453	72	101	10	0:08:32
	2	0. - 0.453	72	101	10	0:08:28
	3	0. - 0.453	72	101	10	0:08:27

^aCPU time on IBM 370/3081, H=OPT2 compiler

ORIGINAL PAGE IS
OF POOR QUALITY

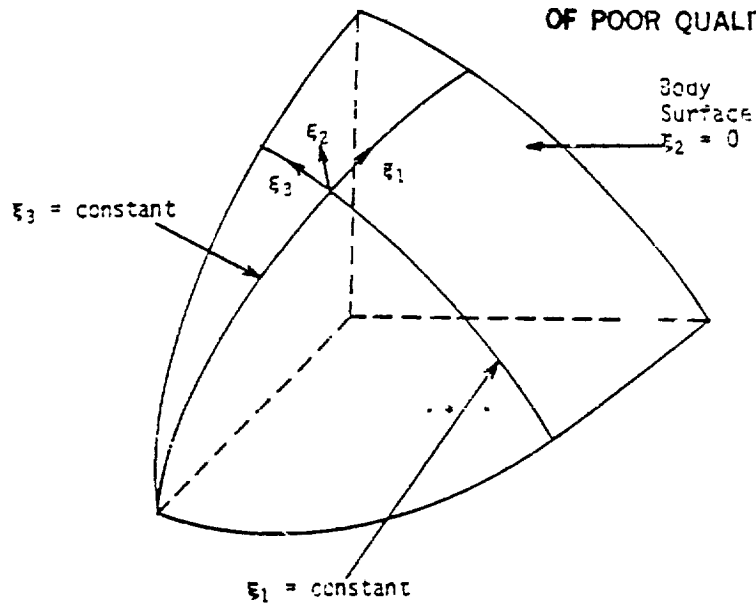


Figure 1.- Body-generator nonorthogonal coordinate system.

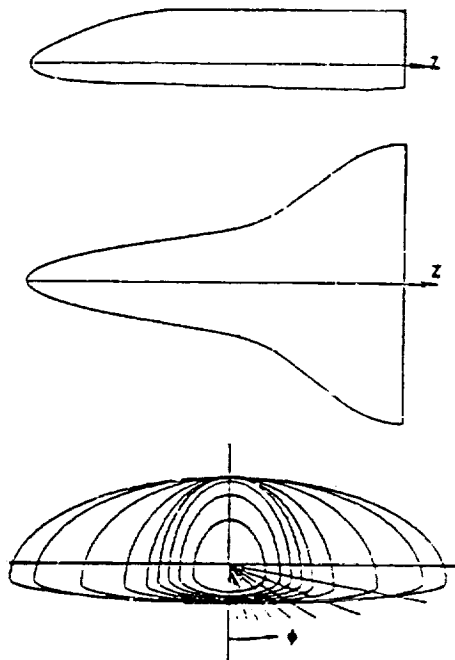


Figure 2.- Cross sections of the modified Shuttle orbiter.

ORIGINAL PAGE IS
OF POOR QUALITY.

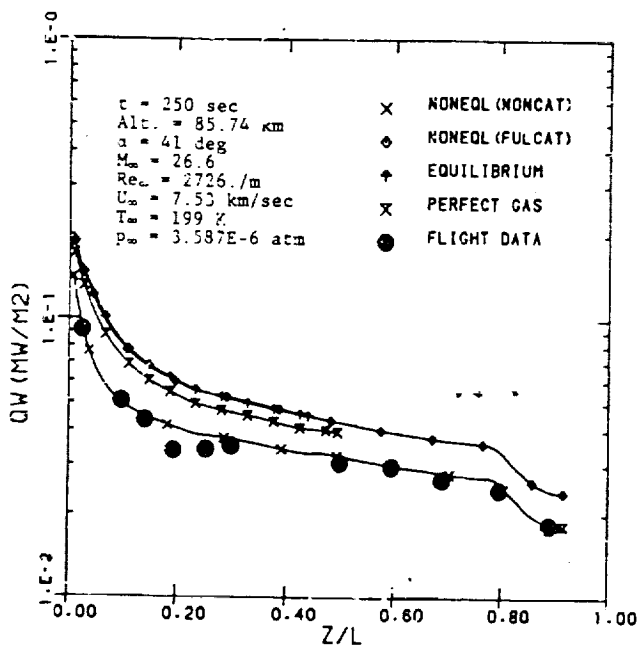


Figure 3.- Comparison of measured and calculated heating rates along the windward centerline of Case 1.

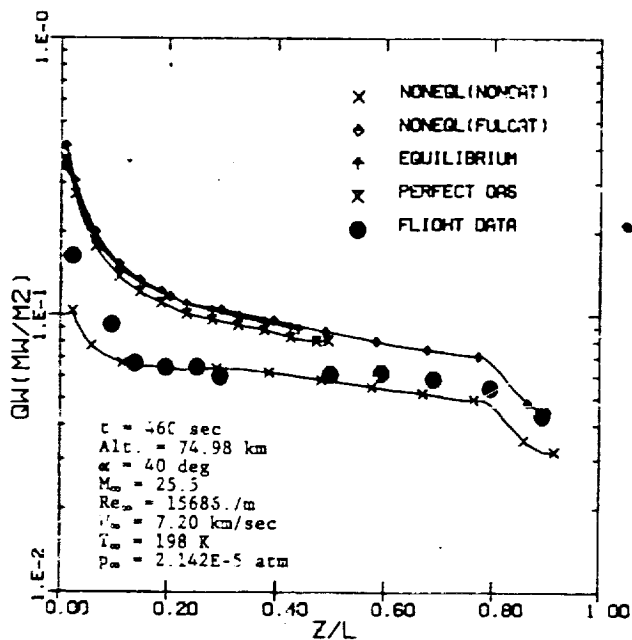


Figure 4.- Comparison of measured and calculated heating rates along the windward centerline of Case 2.

ORIGINAL PAGE IS
OF POOR QUALITY

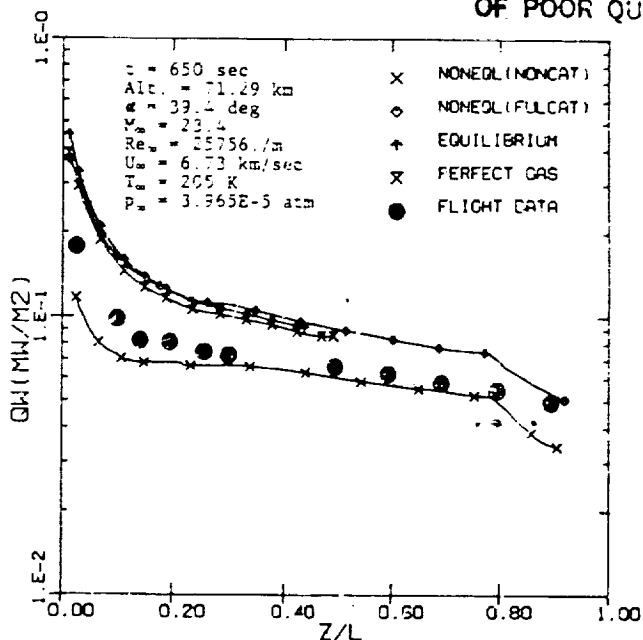


Figure 5.- Comparison of measured and calculated heating rates along the windward centerline of Case 3.

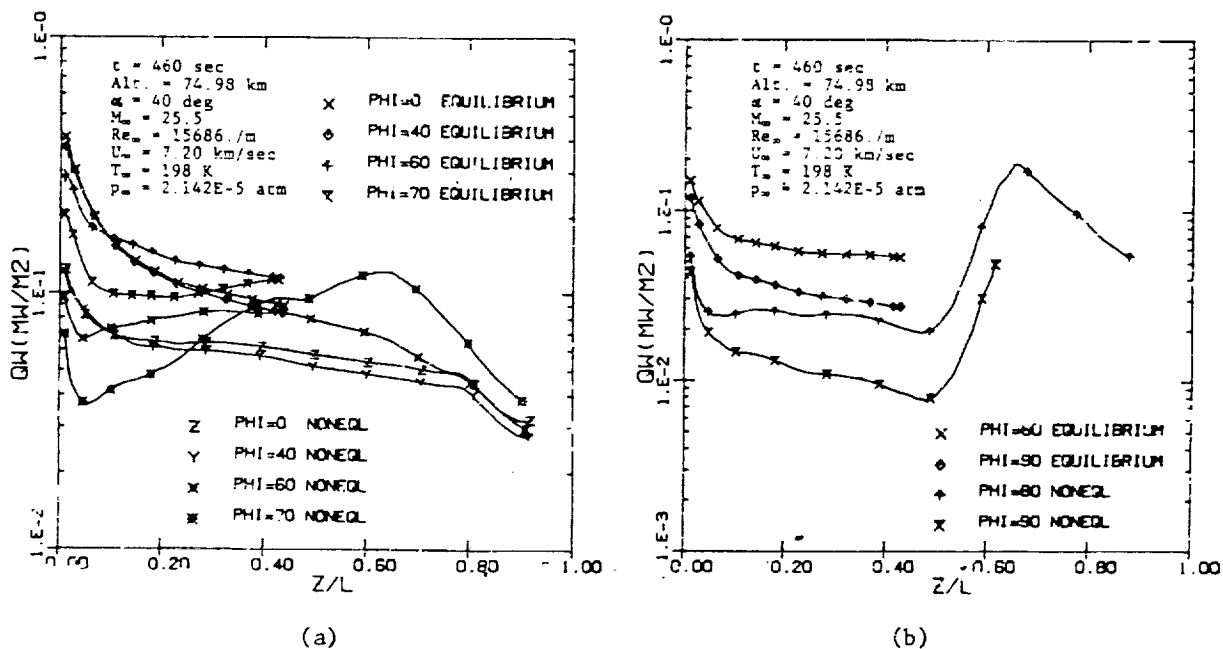
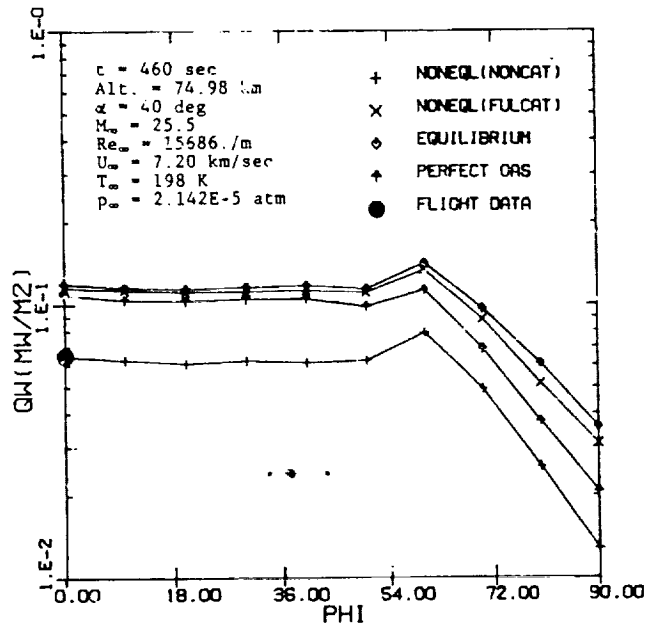
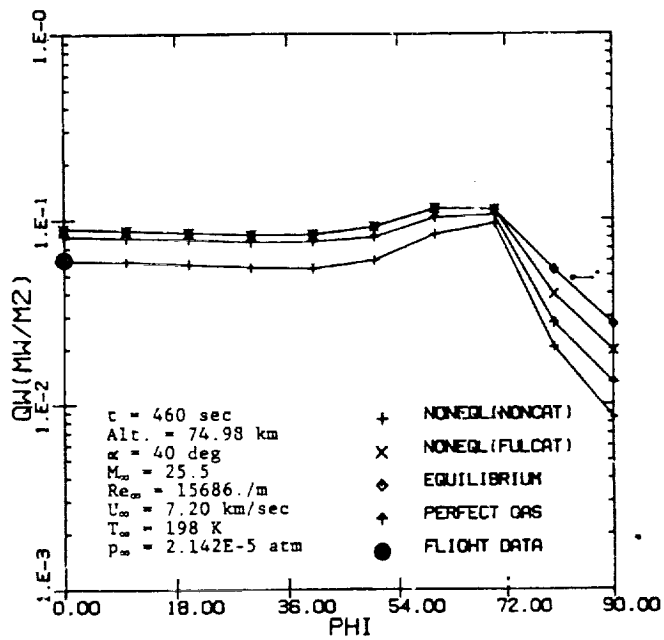


Figure 6.- Surface heating rate distributions along the body for different ϕ -planes of Case 2.

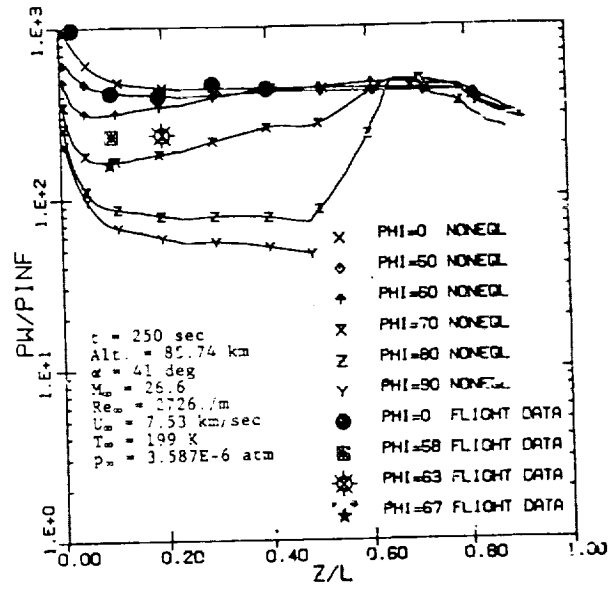


(a) $z/L = 0.20.$

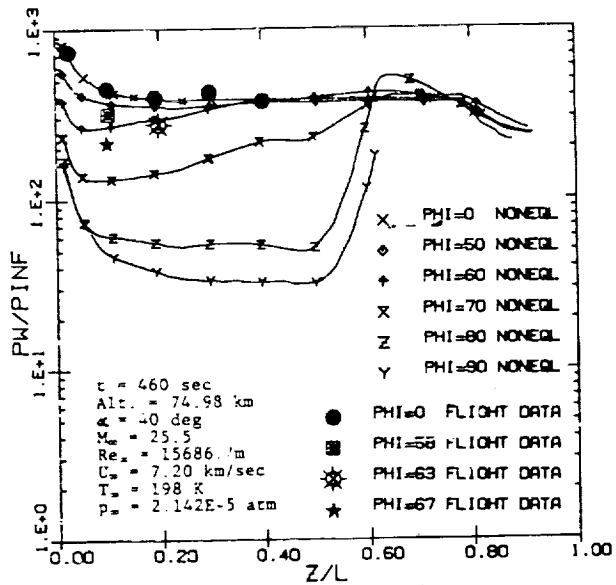


(b) $z/L = 0.44.$

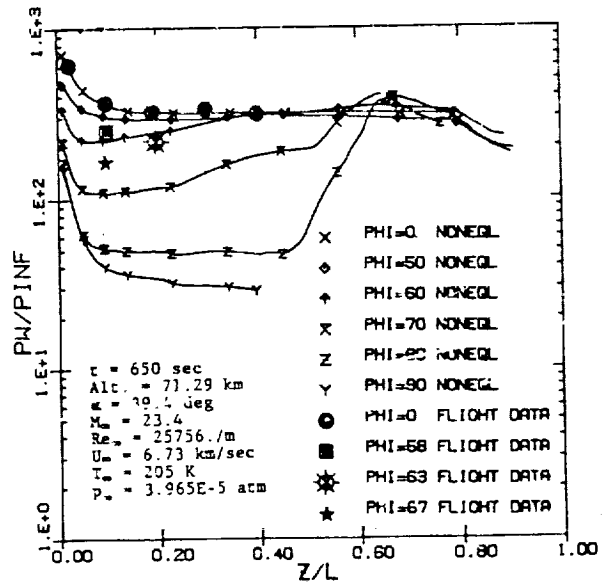
Figure 7.- Spanwise heating rate comparison for Case 2.



(a) Case 1.

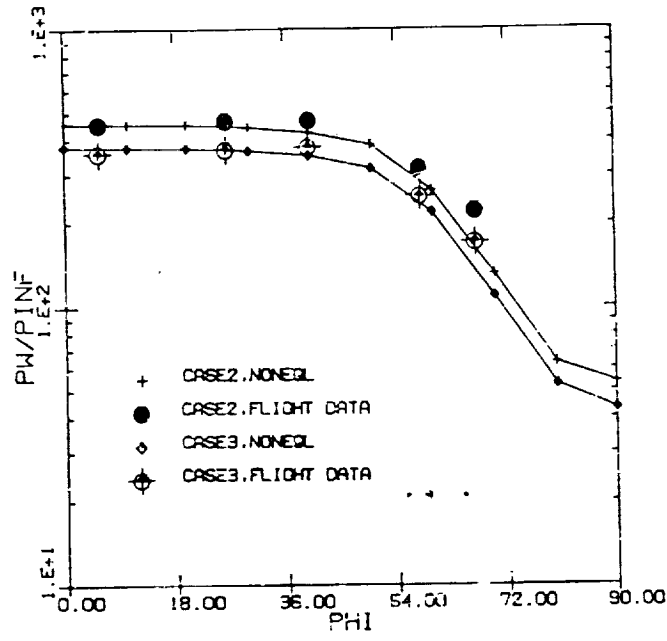


(b) Case 2.

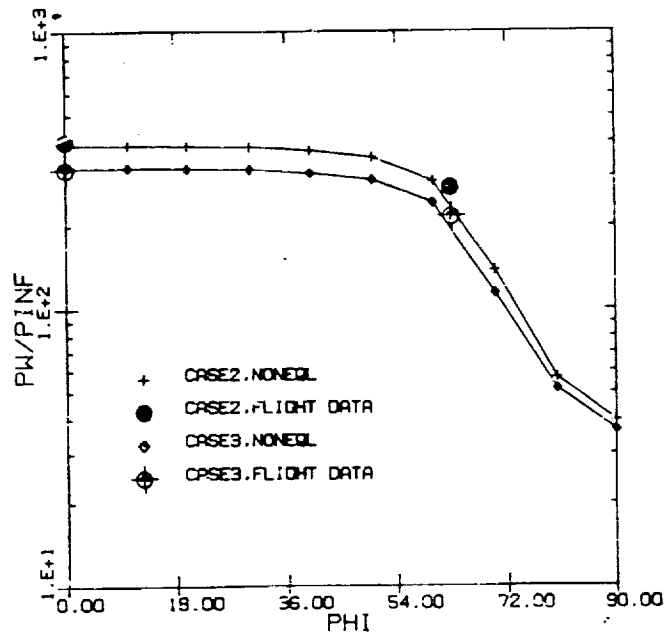


(c) Case 3.

Figure 8.- Comparison of surface pressure distributions along the body.



(a) $z/L = 0.1$.



(b) $z/L = 0.2$.

Figure 9.- Comparison of spanwise surface pressure distributions.

ORIGINAL PAGE IS
OF POOR QUALITY

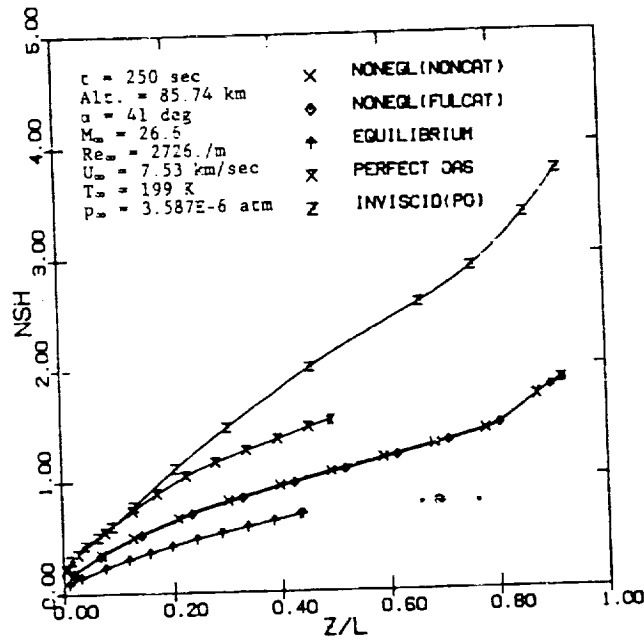


Figure 10.- Comparison of globally iterated shock layer thickness solutions at $\phi = 0$ for Case 1.

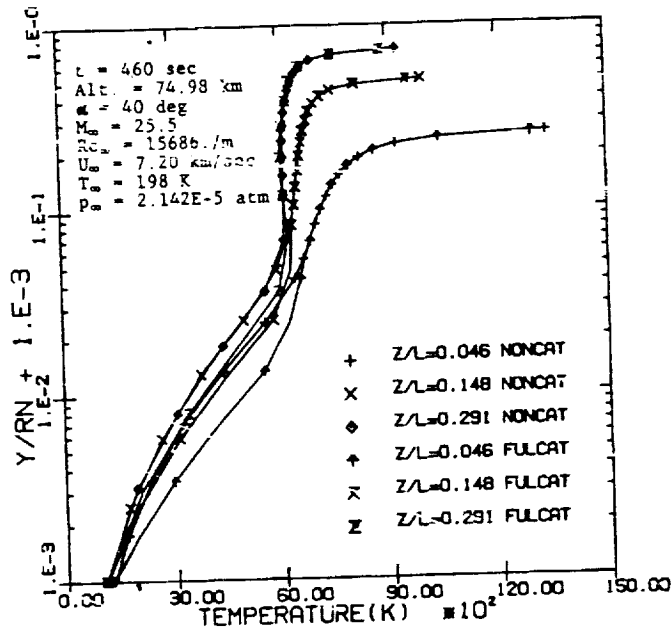


Figure 11.- Shock layer profiles of temperature at various axial body locations along $\phi = 0$ for Case 2.

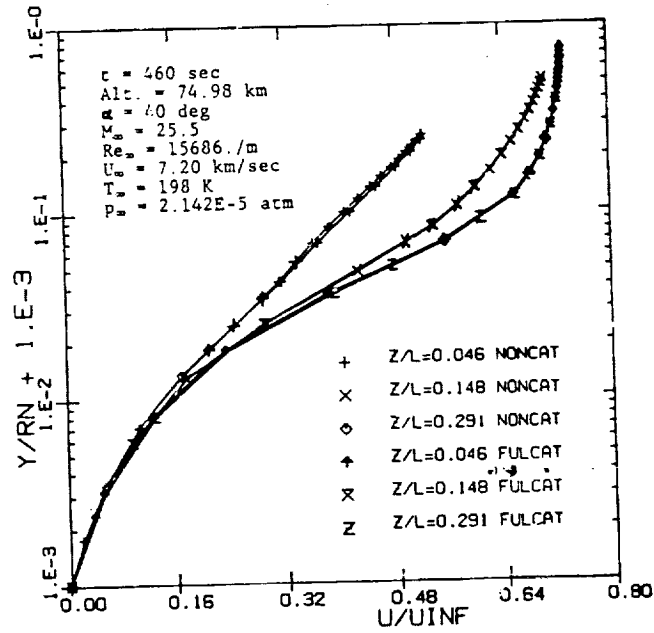


Figure 12.- Shock layer profiles of velocity at various axial body locations along $\phi = 0$ for Case 2.

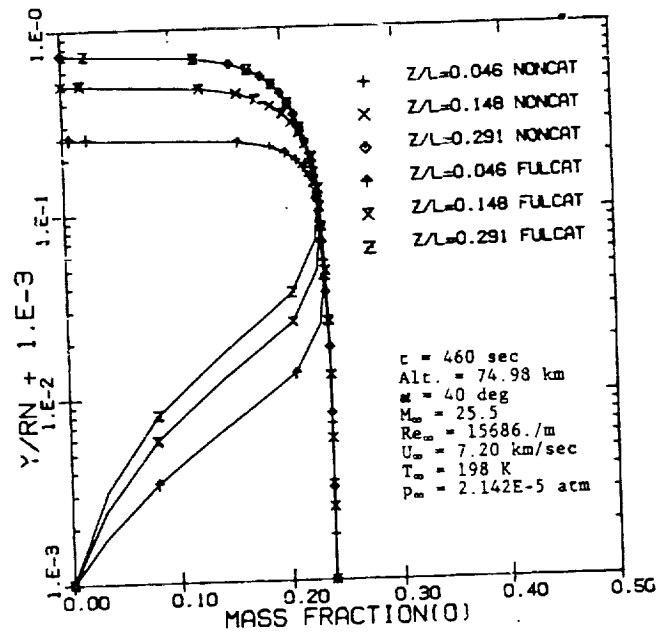


Figure 13.- Shock layer profiles of oxygen mass fraction at various axial body locations along $\phi = 0$ for Case 2.

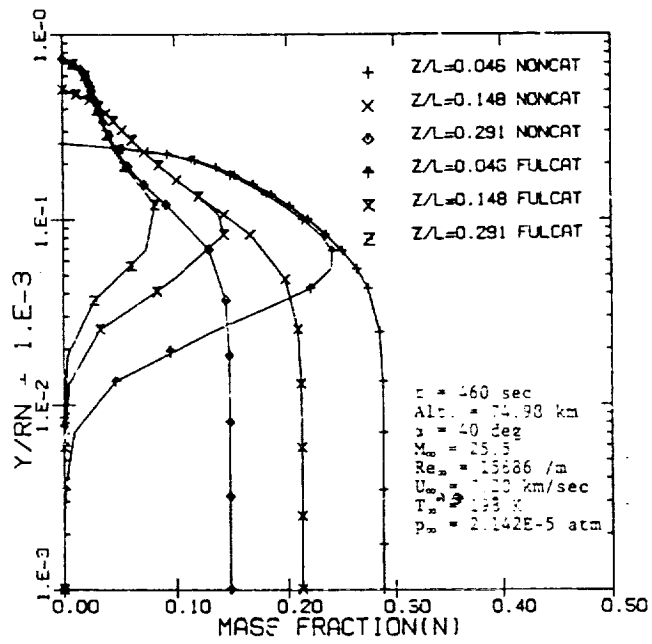


Figure 14.- Shock layer profiles of nitrogen mass fraction at various axial body locations along $\phi = 0$ for Case 2.

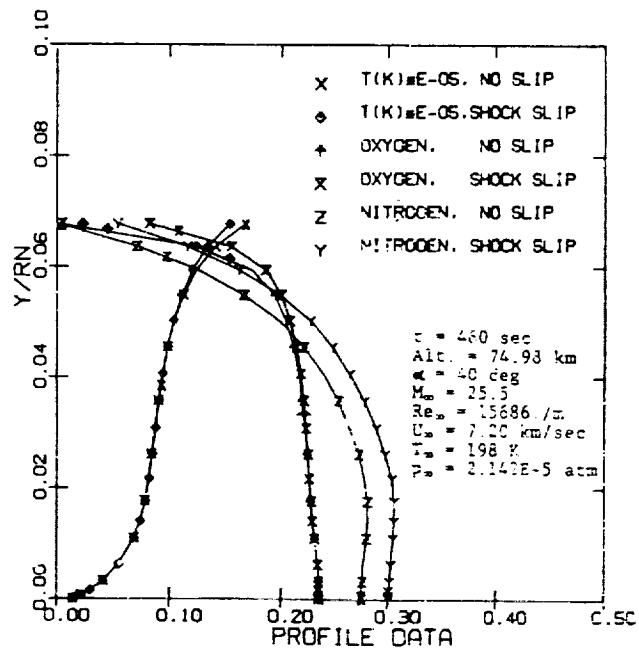


Figure 15.- Shock slip effect on the profile of temperature and mass fraction at stagnation point of Case 2.

ORIGINAL PAGE IS
OF POOR QUALITY

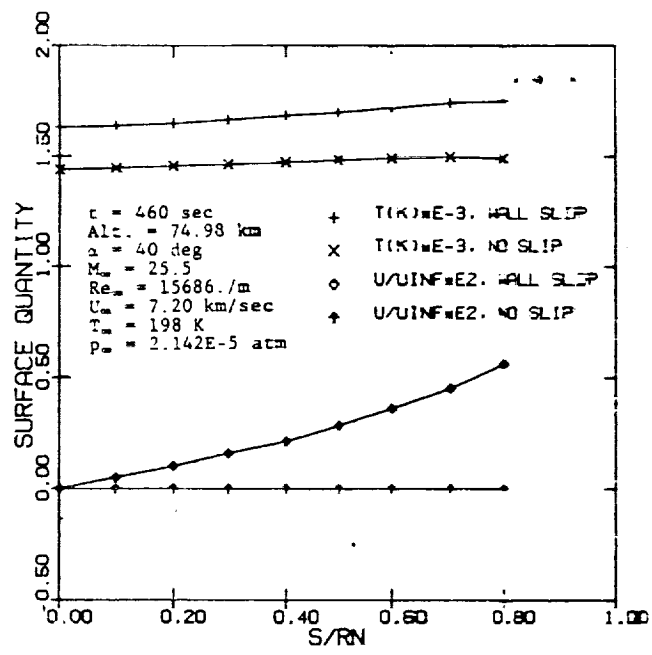


Figure 16.- Wall slip effect on the velocity and temperature jump on the nose region of Case 2.